De Guzman, Mar; Koivumäki, Pasi; Haneda, Katsuyuki

Double-directional Multipath Data at 140 GHz Derived from Measurement-based Ray-launcher

Double-directional Multipath Data at 140 GHz Derived from Measurement-based Ray-launcher

Mar Francis De Guzman*† Pasi Koivumäki * Katsuyuki Haneda*
*Aalto University School of Electrical Engineering, Finland
† Advanced Science and Technology Institute, Department of Science and Technology, Quezon City, Philippines
Email: {francis.deguzman, katsuyuki.haneda}@aalto.fi

Abstract—**The double-directional model of the radio channel is an indispensable tool in the design and evaluation of wireless systems. However, double-directional channel sounding is increasingly more difficult as the carrier frequency increases due to the need to steer narrower antenna beams across azimuth and elevation angles both at transmit (Tx) and receive (Rx) ends, resulting in a huge time duration required for measuring a single Tx-Rx link. To tackle the problem, we utilized a measurement-based ray-launcher (MBRL) to estimate the double-directional path data from single-directional radio channel sounding. The latter performs beam scanning only at one of Tx or Rx ends, allowing us to perform many more Tx-Rx link measurements than double-directional sounding. The MBRL maps multipaths measured from the single-directional channel sounding on a geometry of the measurement site, allowing us to identify the reflection points and angular information of the multipaths that we were not able to measure. Double-directional multipath data covering 12 line-of-sight and 56 non-line-of-sight indoor links at 140 GHz band are the main result of this paper. The data will serve for the design and evaluation of communications links, localization and sensing at 140 GHz.**

I. Introduction

Future generations of wireless systems, i.e., sixth-generation and beyond, are expected to utilize the upper millimeter-wave and Terahertz (THz) band (spanning 0.1-10 THz) to reach even higher data rates on the order of 1 Tbps or more, along with their use for improve device localization and radar as sensing [1]. This motivated the ongoing efforts on propagation channel measurements and channel modelling at the THz band which could support the design and performance evaluation of these systems. Most of the recent studies focus on the understanding of radio channels at above-100 GHz. Links with short distances in indoor scenarios of less than one meter [2], up to four meters [3], up to eight meters [4] and up to 10 m [5], [6] have been investigated. Meanwhile, longer link distances of above 10 m in indoor and outdoor environments were considered in [7]–[11].

One approach to describe the propagation channel is through its double-directional model [12]. The model is particularly relevant in millimeter-wave and Terahertz radios as the electrical size of antennas at link ends becomes larger than legacy sub-6 GHz radios. The double-directional model is derived from channel sounding where both sides of the link has directional antennas or antenna arrays. *Complete* double-directional measurements require mechanical, electrical or offline[1] sweeping of antenna beams at link ends to all possible

angles in turn, which demand expensive and sophisticated antenna systems and their calibration, along with efforts and time to perform the sweeping. The demands become more bottleneck in performing channel sounding when the antenna's half-power beamwidth (HPBW) is narrower.

Double-directional measurements at above-100 GHz frequencies were reported in [8] and [9] using directional antennas at link ends. In [8], a pre-selection of beam scanning angles was applied to reduce the duration of measurements from several days, if complete angular scanning is made over the entire solid angles, to around three hours for a single link between transmit (Tx) and receive (Rx) sides. Double-directional measurements with partial angular scan range at 140 GHz is also performed in [11] where the directional Tx antenna is pointed to a few selected angles while the directional Rx antenna is swept in the whole azimuth in three different elevation angles. A novel alternative method to obtain complete double-directional channel knowledge, which is discussed in this paper, is to complement limited directional measurements through a geometry of the measurement site. The method was called a measurement-based ray-tracer in [13] which was found useful at the sub-6 GHz radio frequency (RF). In this paper, we refer the method as measurement-based ray-launcher (MBRL) as the approach fits closer to the description of ray-launching [14]. A similar approach has been proven to be useful at the millimeter-wave (mm-wave) [15] and Terahertz bands [4] to gain understanding of wave propagation mechanisms. While we in this paper use the MBRL as an efficient way to obtain complete double-directional channel knowledge at 140 GHz. The obtained channel data will be published along with this paper to aid Terahertz radio link designs.

The remainder of the paper is organized as follows. Section II introduces our limited directional channel measurements. Section III discusses the MBRL where wave-reflecting objects are identified in the measurement site and then double-directional channel knowledge is estimated. Section IV presents characteristics of the estimated double-directional channels to demonstrate the efficacy of MBRL. Finally, conclusions are provided in Section V.

II. Single-directional Radio Channel Sounding

A. Channel Sounder

In the single-directional measurements that we analyzed in this paper, one side of the link is equipped with omnidirectional antenna and the other side has directional antenna mounted on

---

[1]offline beam sweeping is realized through signal processing of element-space data to beamspace data by, e.g., the Fourier transform.

a rotator to scan the fixed beam mechanically across different pointing angles. We set the Rx here as the side with directional antenna.

The channel sounder used in the measurements is equipped with Vector Network Analyzer (VNA) and applies swept-frequency method which can obtain the channel response with high delay resolution and dynamic range. We swept 10001 frequency points over 140-144 GHz while the intermediate frequency bandwidth of the VNA was set to 2 kHz. The signals transmitted from and received at the VNA, spanning 1.52-5.52 GHz are translated to RF through frequency converters. The local oscillator (LO) signal at 11.54 GHz for this frequency translation is supplied by a signal generator placed on the Rx side. A radio-over-fibre system which consists of optical-to-electrical and electrical-to-optical converters and a military-grade optical fibre cable with two single-mode fibres distribute the VNA and LO signals. They allow channel measurements with a large Tx-Rx separation distance.

The rotator on the Rx side swept the azimuth angle with $5°$ steps while its broadside was fixed at the $0°$ elevation. The range of azimuth angles covered for each Rx location is represented as red-shaded sectors in Fig. 1. Large walls behind each of Rx locations prevented us from covering the whole $360°$ azimuth range. The height of the Tx and Rx antennas was set to 1.85 m. A 0 dBi omnidirectional bicone antenna with $45°$ elevation HPBW is installed on the Tx side while a 19 dBi horn antenna with $10°$ azimuth HPBW and $40°$ elevation HPBW is on the Rx side. Both antennas primarily radiate and receive the vertical polarization. The effective isotropic radiated power of the Tx was 30 dBm. The observed noise floor at the VNA was around -128 dBm and assuming a margin of 10 dB, the measurable path loss of this channel sounder is 148 dB. Further details on the channel sounder can be found in [16].

B. Channel Sounding

Single-directional measurements were performed in the entrance hall of the Electrical Engineering building of Aalto University in Finland. Most of the areas have high ceilings and some have single floor ceilings. The sides are composed of concrete and metallic walls, and glass walls with metallic frames as a partition to office spaces. Most prominent objects found in the area are metallic cylindrical columns, staircases, lockers, glass partitions, chairs and tables. The glass partitions are mostly transparent but also have some sections that are opaque. There are no moving objects during the measurements. A map of the area and the antenna locations are shown in Fig. 1. There are three Rx locations and 25 Tx locations, and all possible Tx-Rx combinations were measured except for Tx5-Rx1, Tx6-Rx1, Tx0-Rx2, Tx1-Rx2, Tx24-Rx2, Tx0-Rx3, Tx1-Rx3, and Tx4-Rx3. Out of the total 68 links, 12 are line-of-sight (LOS) and 56 are non-line-of-sight (NLOS). Before the over-the-air measurements, a back-to-back (B2B) measurement was first performed by connecting a 30 dB attenuator between the RF ports of the upconverter and downconverter. Fifty frequency sweeps of this B2B setup are collected and applied during the post-processing of the measured channel response. This calibration process de-embeds the effect of the sounder components in the measured channel response.

From measurements of a single Tx-Rx link, a power

angular-delay (PADP) profile is obtained. It can be characterized by the sum of discrete multipaths as [7], [10]

$$P(\phi, \tau) = \sum_{n=1}^{N} G_n \delta\left(\phi - \phi_n'^{\text{Rx}}\right) \delta\left(\tau - \tau_n\right), \qquad (1)$$

where N is the number of paths, G_n, $\phi_n'^{\text{Rx}}$, and τ_n are the gain, measured azimuth angle-of-arrival (AoA), and delay of the nth path, respectively. As the broadside of the directional antenna was fixed at the $0°$ elevation during measurements, we also lack of resolved elevation angles of paths on the Rx side. Antenna gains are de-embedded in (1) using radiation patterns of the horn and bicone antennas.

III. MEASUREMENT-BASED RAY-LAUNCHER (MBRL)

The MBRL is different from an ordinal ray-launching in that rays are launched from antenna locations *only to the directions where multipath were observed in measurements*. Availability of directional channel measurements is therefore a pre-requisite when using the MBRL. The MBRL yields reflection points of measured multipaths in the environment and their AoAs and angle-of-departures (AoDs).

A. Input Data to MBRL

In order to run the MBRL, detailed geometric database of the measurement site from laser scanning, also called point cloud data, has been used, similarly to [15], [17]. Since it can capture physical objects with millimeter accuracy, its use is becoming more relevant for mm-wave and Terahertz bands where smaller details of objects can influence the reflection and scattering of radio waves. The point cloud was pre-processed for the MBRL such that local surfaces were formed by a group of points and their normal vectors were derived [17]. The point cloud was *not* converted to a mesh model to avoid losing details of the environment.

Other required inputs to the MBRL are the antenna locations during channel sounding and spatio-temporal parameters of measured paths in (1), i.e., the azimuth AoA, and propagation delays. As the limited single-directional channel sounding does not offer path elevation estimates at the Rx, rays are launched from the Rx location $\boldsymbol{r}^{\text{Rx}}$ at the exact measured azimuth estimate as well as at directions around the exact angle, as illustrated in Fig. 2. The ellipse defined on the azimuth-elevation domain represents the main lobe of the directional antenna used in the measurements, and hence is also related to uncertainty of the measured path angular estimates. In the following, we explicitly use terms *paths* and *rays* to mean different things: the former is from observations of measurements as evidence of the reality, while the latter refers to a group of lines launched from the antenna location in the MBRL, illustrated in Fig. 2, for each of measured paths.

B. Identification of Reflection Points

A launched ray from the Rx antenna location follows its straight trajectory until it interacts with a local surface in the point cloud. Specular reflections are the only propagation mechanism implemented in this MBRL. Upon hitting a local surface, the direction of the reflected ray is calculated by
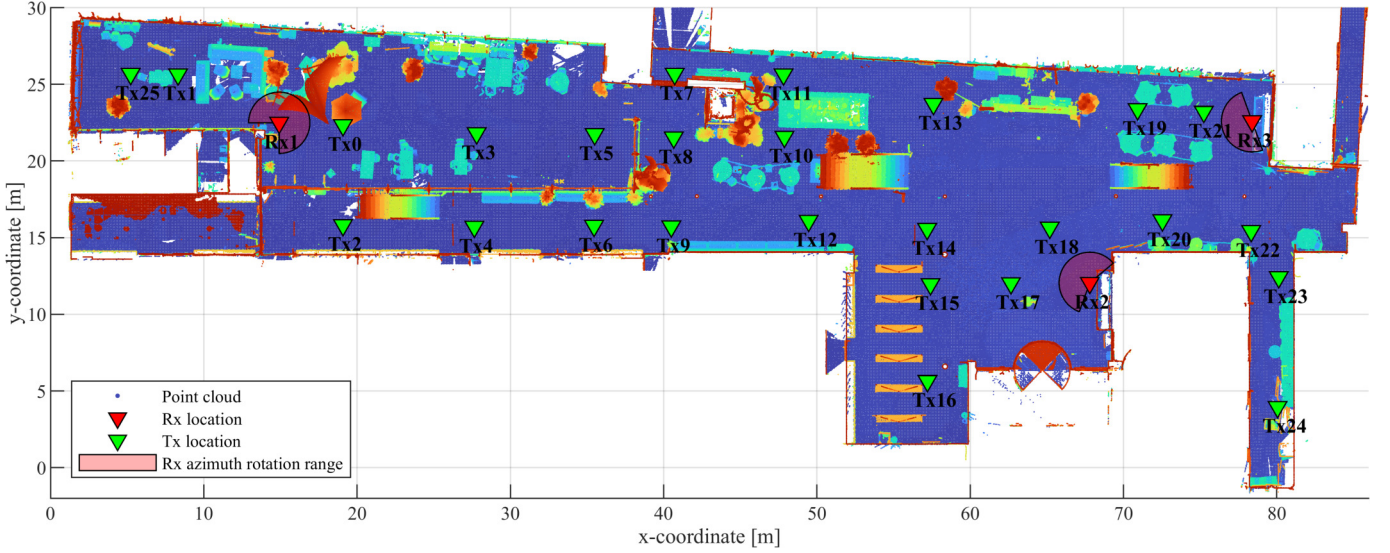
Fig. 1. A top view of a point cloud map of the entrance hall. Antenna locations, and azimuth rotation range of the Rx antenna are overlaid.
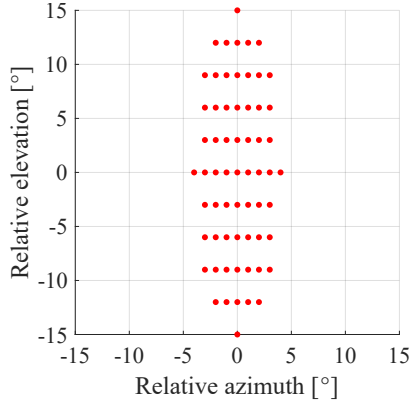

Fig. 2. The ellipsoid on the azimuth-elevation domain that defines the angular range where rays are launched from the Rx antenna location in the point cloud; 0 deg corresponds to the angular estimate of a path from channel sounding.

applying the Snell's law of reflection. Similar to [15], all the near-by local surfaces that reside in the first Fresnel zone of the ray contribute to the reflection and considered as the secondary sources of the reflected rays according to the Huygens principle. The mth ray of nth path continues to traverse until the ray length corresponds to the measured delay τ_n. The endpoint of the ray is denoted as $r'^{\mathrm{RT}}_{m,n}$. A path is said to be successfully mapped on the geometry if it has at least one launched ray having an endpoint sufficiently close to the actual Tx location r^{Tx}, fulfilling $\delta_{\mathrm{R}} < R_{\mathrm{th}}$; δ_{R} is the distance error equal to $\|r^{\mathrm{Tx}} - r^{\mathrm{RT}}_{m,n}\|$ and R_{th} is the distance error threshold. The rays that satisfy this condition are referred here as candidate rays, and the successfully mapped paths on the geometry as traversed paths. The pth candidate endpoint is denoted here as $r^{\mathrm{RT}}_{p,n} = \left[x^{\mathrm{RT}}_{p,n}, y^{\mathrm{RT}}_{p,n}, z^{\mathrm{RT}}_{p,n}\right]$. The points in the point cloud that contribute to the reflection of the candidate rays are collected as candidate reflection points for each path. The reflection points of the pth ray is denoted here as a position vector $r^b_{p,n} = \left[x^b_{p,n}, y^b_{p,n}, z^b_{p,n}\right]$, $1 \le b \le B$ where b is the order of reflection as the ray traverses from the Rx antenna location; $r^B_{p,n}$ is the last interacting reflection point. In this

work, only up to second order reflections are considered so that $B \le 2$.

C. Estimation of Tx and Rx Path Angles Information

Similarly, the angles where the candidate rays are launched from the Rx location become the candidate AoA estimates $\boldsymbol{\Omega}^{\mathrm{Rx}}_{p,n} = \left[\phi^{\mathrm{Rx}}_{p,n}, \psi^{\mathrm{Rx}}_{m,n}\right]$. The corresponding AoD estimates $\boldsymbol{\Omega}^{\mathrm{Tx}}_{p,n} = \left[\phi^{\mathrm{Tx}}_{p,n}, \psi^{\mathrm{Tx}}_{p,n}\right]$ are obtained by calculating the direction of the last interacting reflection points seen from the Tx location, i.e.

$$\phi^{\mathrm{Tx}}_{p,n} = \arctan\left(y^{\mathrm{TB}}_{p,n}/x^{\mathrm{TB}}_{p,n}\right), \quad (2)$$

$$\psi^{\mathrm{Tx}}_{p,n} = \arctan\left(z^{\mathrm{TB}}_{p,n}/\sqrt{(x^{\mathrm{TB}}_{p,n})^2 + (y^{\mathrm{TB}}_{p,n})^2}\right), \quad (3)$$

where $r^{\mathrm{TB}}_{p,n} = \left[x^{\mathrm{TB}}_{p,n}, y^{\mathrm{TB}}_{p,n}, z^{\mathrm{TB}}_{p,n}\right] = r^B_{p,n} - r^{\mathrm{Tx}}$. It can be inferred that multiple angle and reflection point estimates are generated for each measured path when multiple candidate rays are obtained. The following steps are applied to find the most probable estimate out of them. The estimates are first clustered by applying the density-based spatial clustering of applications with noise (DBSCAN) [18]. It is assumed sufficient to cluster only the coordinate estimates of the last reflection point $r^B_{p,n}$ and apply the same grouping to other estimates such as AoA and AoD. The next step is to assign to each estimate a heuristic weight w given by

$$w = \begin{cases} -\beta_1\delta_R + 1 & 0 \le \delta_R < 0.5 \\ (-0.5\beta_1 + 1)e^{-\beta_2(\delta_R - 0.5)} & 0.5 \le \delta_R < 1.0, \end{cases}$$

where β_1 and β_2 are the linear and exponential decay factors, respectively. The weight function decreases with increasing distance error at endpoints of candidate rays. Large weights are given to rays with small distance errors as the error is only most likely due to inaccuracy in measured antenna locations. While small weights result from the exponential decay for rays having large distance errors. Then a cluster of candidate rays with the highest total weights is selected as the most likely cluster of rays. Unique estimates of angles and path reflection coordinates are derived for the cluster by calculating
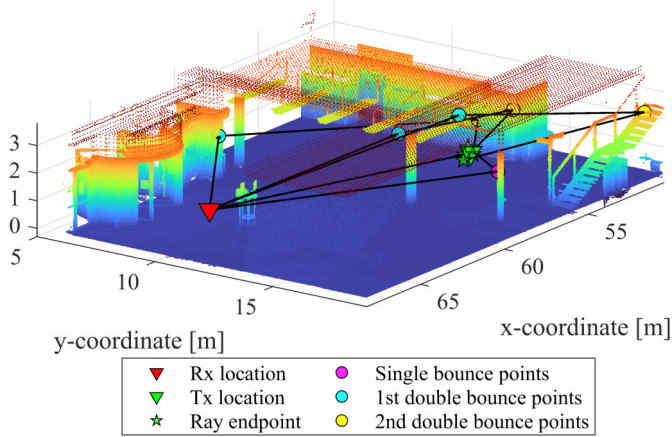
Fig. 3. Exemplary traversed paths and identified reflection points for the Rx2-Tx14 link.
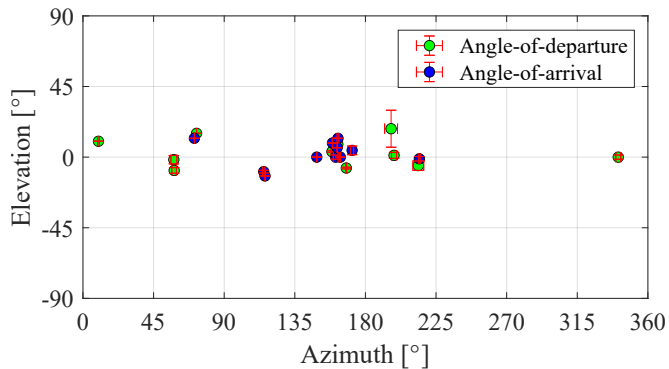

Fig. 4. Estimated angles-of-departure and angles-of-arrival in azimuth and elevation domains of Rx2-Tx14 link using the measurement-based ray-launcher. Error bars associated to each path plot represent the standard deviation of angular estimates in the respective domains.

the weighted mean of the angles and path reflection coordinates of candidate rays in the selected cluster. The weighted standard deviation of the ray parameters is also derived for the same cluster as a uncertainty measure. Circular mean and circular standard deviation are applied in the azimutal domain.

IV. CHARACTERISTICS OF TRAVERSED PATHS

The MBRL was run with the center frequency of 142 GHz. The rays were launched from the Rx for a path across the azimuth and elevation ranges of $\pm 4°$ and $\pm 15°$ at every $1°$ and $3°$, respectively; see the ellipse in Fig. 2. The ellipse was centered at the path azimuth estimate from the measurement and at $0°$ elevation. The distance threshold was $R_{\mathrm{th}} = 1.0$ m. The point cloud data was downsampled using grid average downsample method to a resolution of 10 cm.

A. Physical Attributes of Paths

An exemplary illustration of traversed paths for Rx2-Tx14 link is shown in Fig. 3. Only a portion of the paths and reflection points of the mentioned link are shown for clarity. The reflection points are found on the metallic entrance door frame, metallic locker, wall, ceilings, metallic column, and metallic staircase. It was found that 92% of the traversed paths undergo double bounce reflections. The most prominent
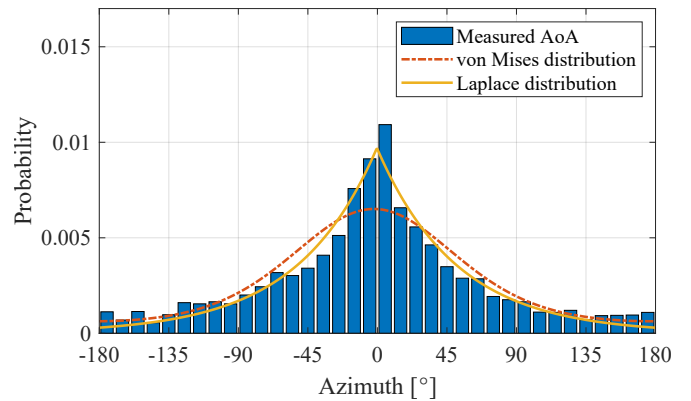

Fig. 5. Normalized histogram of measured azimuth angles-of-arrival and fitted distribution curves.

reflecting objects include large planar surfaces such as floors, ceilings, walls, and opaque sections of glass partitions, and curved surfaces such as cylindrical building columns and the steel frames of the revolving door. A small portion of the reflection points are found on the staircases, chairs, and tables.

B. Angular Estimates

Exemplary path estimates of AoA and AoD from the MBRL for Rx2-Tx14 link are illustrated in Fig. 4. The center of each marker denotes the mean while the error bar represents the standard deviation of each traversed path as discussed in Sec. III-C. In most paths, the standard deviation is almost negligible. It can also be noticed that the estimates are concentrated on the horizontal plane which is expected for a link with equal Tx and Rx antenna heights.

C. AoA and AoD Statistics

The normalized histogram of the measured azimuth AoA is plotted in Fig. 5. In deriving the histogram, the path angles were normalized to the direction of the Tx antenna in each link, both in LOS and NLOS channels. Furthermore, the LOS paths were excluded in deriving the histogram. Still the azimuth AoAs of measured paths are seen to be concentrated at azimuth equal to $0°$, i.e., the direction of the optical LOS.

The histogram was fitted with the von Mises and Laplace distributions. The former is the circular analog of the normal distributions used for linear data, given by

$$f\left(\alpha \mid \mu_{\mathrm{v}}, \kappa\right) = \frac{1}{2\pi I_0(\kappa)} \exp\left(\kappa \cos\left(\alpha - \mu_{\mathrm{v}}\right)\right) \quad (4)$$

where α is the angular data, μ_{v} is the mean, κ is the concentration parameter, and $I_0(\cdot)$ is the modified Bessel function of order 0; the inverse of the concentration parameter $1/\kappa$ is analogous to the variance of the normal distribution. Laplace distribution is also considered here as it generally has good fit for angular data with a sharp peak. It is defined by

$$f(\alpha \mid \mu_{\mathrm{l}}, b) = \frac{1}{2b} \exp\left(-\frac{|\alpha - \mu_{\mathrm{l}}|}{b}\right) \quad (5)$$

where the location and scale parameters are denoted as μ_{l} and b, respectively; the latter is proportional to the standard deviation.
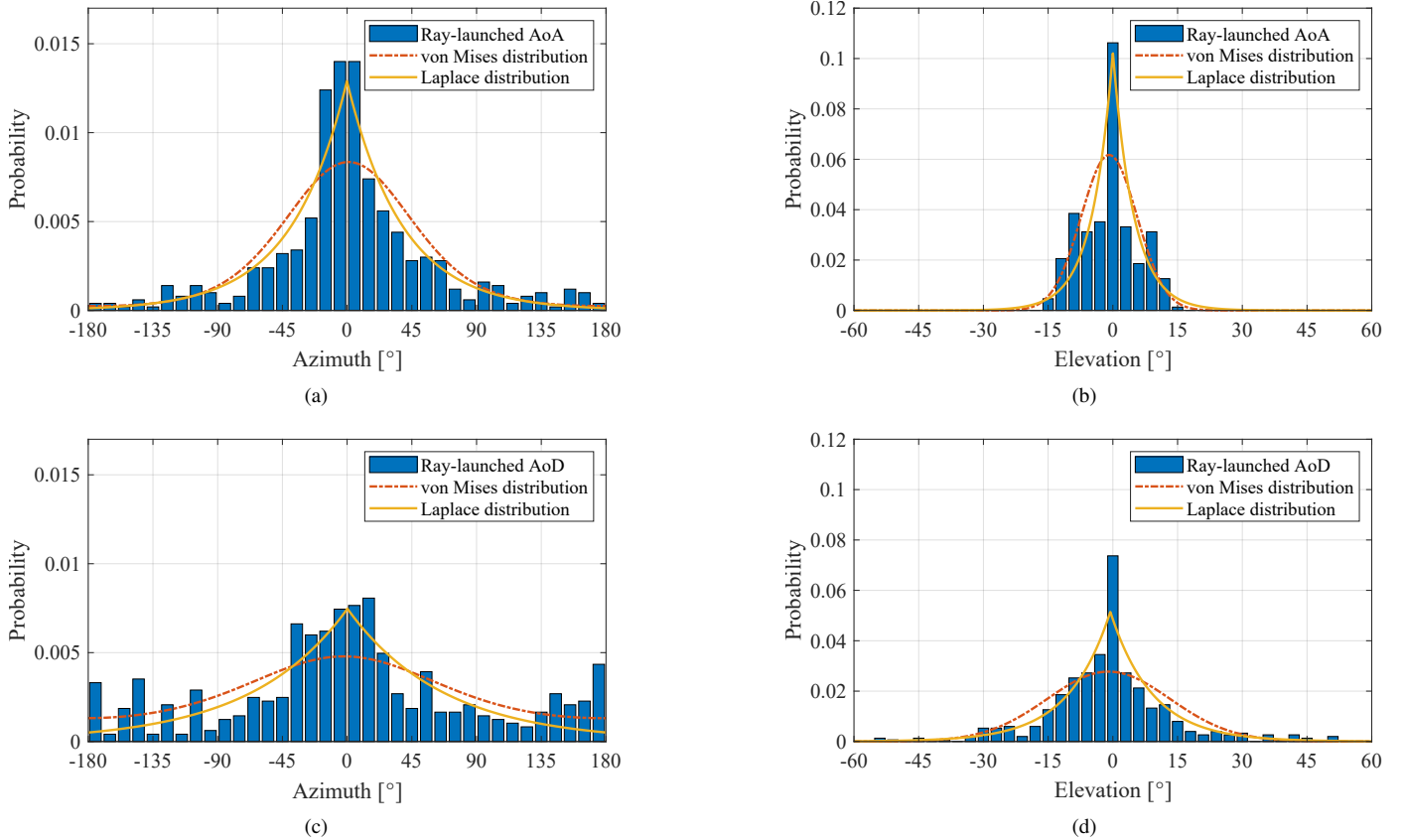
Fig. 6.   Normalized histogram and fitted distribution curves for ray-launched (a) Azimuth angles-of-arrival (b) Elevation angles-of-arrival (c) Azimuth angles-of-departure (d) Elevation angles-of-departure.

TABLE I.   DISTRIBUTION PARAMETERS OF MEASURED AND RAY-LAUNCHED ANGLES.

Parameter		von Mises		Laplace	
		μ_v [°]	κ [a.u.]	μ_l [°]	b [°]
Measured AoA	Azimuth	−2.3	0.02	−0.3	51.5
Ray-launched AoA	Azimuth	1.0	0.03	−0.1	38.8
	Elevation	−0.9	1.37	0.0	4.9
Ray-launched AoD	Azimuth	−2.3	0.01	0.2	67.0
	Elevation	−1.0	0.28	−0.59	9.7

The distribution fits show that the Laplace distribution provides better fit to the empirical histogram especially at the center angle. The same curves for different angles for traversed paths in MBRL are plotted in Fig. 6. When comparing Fig. 6(a) and 5, the AoA histograms show a good agreement. Fewer paths are naturally found in the rear direction, i.e. azimuth= $180°$ in the histogram of the azimuth AoA than azimuth AoD, due to the limited azimuth AoA range of the Rx antenna scanning as discussed in Sec. II. Meanwhile, elevation histograms of the ray-launched AoA and AoD estimates have similar shape where the reference angle, i.e., elevation= $0°$, is highly concentrated and the tails are light. This shape may be attributed to the equal antenna heights of the link, large link distances, and the limited elevation HPBW of the antennas. Finally, the best-fit parameters of the distribution functions to the histograms are listed in Table I. While all the mean azimuth estimates are close to $0°$, the scale parameters show smaller spread for elevation than azimuth domains.

D. Path Mapping Success Rate

Efficacy of the MBRL was assessed by comparing the totality of paths that were successfully mapped on the geometry of the measurement site to that of measured paths. The totality refers to 1) the total number of paths and 2) total power of the link. The number of paths are shown as bar plots in Fig. 7, showing that around 70% of the measured paths in each link on average were successfully mapped on the geometry using the MBRL. The power percentage of successfully mapped paths in each link is also illustrated in Fig. 7 as stem plots. It was found that about 84% of the total power in each link was successfully mapped on the geometry of the site on average. It must be noted that several links without the bar and stem plots correspond to the link outage where no path was observed in the channel sounding.

Measured paths that were not mapped on the geometry can be attributed to different reasons, e.g., 1) transparent portions of glass walls that were not captured during laser scanning; 2) propagation mechanisms that were not implemented in the MBRL such as higher order reflections, transmission and diffraction. These limitation will be addressed for improving the MBRL in the future.

V.   CONCLUSION

We demonstrated the derivation of the double-directional multipath data of an indoor environment at 140 GHz. The
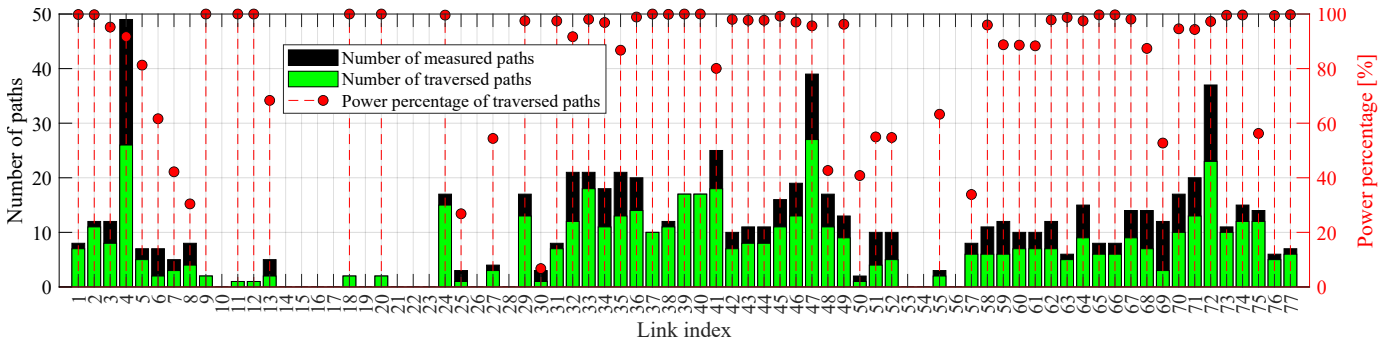
Fig. 7. Number of measured and traversed paths, and power percentage of traversed paths for each measurement link.

derivation complements the data obtained from extensive single-directional measurements. A detailed description of the map in the form of the point cloud allowed accurate projection of the measured paths on various reflection objects. Majority of them are large flat surfaces such as floors, walls, ceilings, and opaque glass partitions, and on curved surfaces such as cylindrical building columns and steel frames of the revolving door. Considering up to double bounce specular reflections in the MBRL allowed us to map most of the measured paths onto the geometry of the measurement site. Histograms of path AoAs and AoDs both in the azimuth and elevation domains are found concentrating at the reference direction pointing to the other link ends. The presented process in extracting the double-directional data is implicitly spatially-consistent geometrical modeling of channels. The double-directional path data estimated from the MBRL, covering 12 LOS and 56 NLOS links, are published in [19] to aid analyses of communication, localization and sensing at 140 GHz band.

REFERENCES

[1] M. Leinonen et al., "Deliverable D2.2 Initial radio models and analysis towards ultra-high data rate links in 6G," 2021. [Online]. Available: https://hexa-x.eu/deliverables/

[2] S. Kim, W. T. Khan, A. Zajić, and J. Papapolymerou, "D-band channel measurements and characterization for indoor applications," *IEEE Transactions on Antennas and Propagation*, vol. 63, no. 7, pp. 3198–3207, 2015.

[3] B. De Beelde, D. Plets, E. Tanghe, and W. Joseph, "Directional sub-THz antenna-channel modelling for indoor scenarios," in *2021 15th European Conference on Antennas and Propagation (EuCAP)*, 2021, pp. 1–4.

[4] Y. Chen, Y. Li, C. Han, Z. Yu, and G. Wang, "Channel measurement and ray-tracing-statistical hybrid modeling for low-terahertz indoor communications," *IEEE Transactions on Wireless Communications*, vol. 20, no. 12, pp. 8163–8176, 2021.

[5] L. Pometcu and R. D'Errico, "An indoor channel model for high data-rate communications in d-band," *IEEE Access*, vol. 8, pp. 9420–9433, 2020.

[6] Y. Lyu, P. Kyösti, and W. Fan, "Sub-THz vna-based channel sounder structure and channel measurements at 100 and 300 GHz," pp. 1–5, 2021.

[7] S. L. H. Nguyen, J. Järveläinen, A. Karttunen, K. Haneda, and J. Putkonen, "Comparing radio propagation channels between 28 and 140 GHz bands in a shopping mall," in *12th European Conf. Ant. Prop. (EuCAP 2018)*, 2018, pp. 1–5.

[8] N. A. Abbasi, A. Hariharan, A. M. Nair, A. S. Almaiman, F. B. Rottenberg, A. E. Willner, and A. F. Molisch, "Double directional channel measurements for THz communications in an urban environment," in *ICC 2020 - 2020 IEEE International Conference on Communications (ICC)*, 2020, pp. 1–6.

[9] N. A. Abbasi, J. Gomez-Ponce, D. Burghal, R. Kondaveti, S. Abu-Surra, G. Xu, C. Zhang, and A. F. Molisch, "Double-directional channel measurements for urban THz communications on a linear route," in *2021 IEEE Int. Conf. Commun. Works. (ICC Workshops)*, 2021, pp. 1–6.

[10] S. L. H. Nguyen, K. Haneda, J. Järveläinen, A. Karttunen, and J. Putkonen, "Large-scale parameters of spatio-temporal short-range indoor backhaul channels at 140 GHz," in *2021 IEEE 93rd Vehicular Technology Conference (VTC2021-Spring)*, 2021, pp. 1–6.

[11] S. Ju and T. S. Rappaport, "140 GHz urban microcell propagation measurements for spatial consistency modeling," in *ICC 2021 - IEEE Int. Conf. Commun.*, 2021, pp. 1–6.

[12] M. Steinbauer, A. Molisch, and E. Bonek, "The double-directional radio channel," *IEEE Antennas and Propagation Magazine*, vol. 43, no. 4, pp. 51–63, 2001.

[13] J. Poutanen, K. Haneda, J. Salmi, V.-M. Kolmonen, A. Richter, P. Almers, and P. Vainikainen, "Development of measurement-based ray tracer for multi-link double directional propagation parameters," in *2009 3rd European Conf. Ant. Prop.*, 2009, pp. 2622–2626.

[14] A. F. Molisch, *Wireless Communications*. Wiley, 2011.

[15] U. T. Virk, S. L. H. Nguyen, K. Haneda, and J.-F. Wagen, "On-site permittivity estimation at 60 GHz through reflecting surface identification in the point cloud," *IEEE Transactions on Antennas and Propagation*, vol. 66, no. 7, pp. 3599–3609, 2018.

[16] M. F. De Guzman, M. Hassan, and K. Haneda, "Uncertainty of millimeter-wave channel sounder due to integration of frequency converters," in *Proc 2021 17th Int. Symp. Wireless Commun. Sys. (ISWCS)*, 2021, pp. 1–6.

[17] P. Koivumäki, G. Steinböck, and K. Haneda, "Impacts of point cloud modeling on the accuracy of ray-based multipath propagation simulations," *IEEE Transactions on Antennas and Propagation*, vol. 69, no. 8, pp. 4737–4747, 2021.

[18] M. Ester, H.-P. Kriegel, J. Sander, and X. Xu, "A density-based algorithm for discovering clusters in large spatial databases with noise," in *Proc. Second International Conference on Knowledge Discovery and Data Mining*, ser. KDD'96. AAAI Press, 1996, p. 226–231.

[19] M. F. de Guzman and K. Haneda, "Measured double-directional multipath data in an indoor entrance hall environment at 140 GHz," 2022. [Online]. Available: https://zenodo.org/communities/hexa-x/